Geophysical Journal International

Geophys. J. Int. (2023) **234,** 228–242
Advance Access publication 2023 February 14
GJI Seismology

https://doi.org/10.1093/gji/ggad066

A note on Marchenko-linearised full waveform inversion for imaging

Leon Diekmann,[1] Ivan Vasconcelos[1] and Tristan van Leeuwen[2,3]

[1]*Department of Earth Sciences, Utrecht University, Princetonlaan 8A,* 3584 *CB, Utrecht, the Netherlands. E-mail: l.d.diekmann@uu.nl*
[2]*Department of Mathematics, Utrecht University, Budapestlaan 6,* 3584 *CD, Utrecht, the Netherlands*
[3]*Centrum Wiskunde & Informatica, Science Park* 123, 1098 *XG, Amsterdam, the Netherlands*

Accepted 2023 February 7. Received 2023 February 6; in original form 2022 November 26

SUMMARY

Full waveform inversion and least-squares reverse time migration are the leading technologies for imaging with seismic waves. Both of them usually rely (in one way or another) on a single-scattering approximation, i.e. the Born approximation, to compute gradients and obtain an updated model. This approximation linearises the relation between modelled data and model by ignoring multiple scattering. We propose to use the Marchenko integral, an equation originating from inverse scattering theory, to obtain an alternative linear equation. Using the Marchenko method we can retrieve Green's functions, including all orders of scattering, for virtual sources anywhere within the volume of interest – without prior knowledge of the high-wavelength model variations that induce scattering. Plugging these estimated Green's functions into the Lippmann–Schwinger integral delivers a Marchenko-linearised relation between the full waveform data and the model. We present this new linearisation strategy and illustrate its advantages and disadvantages by comparing numerical results for different inversion kernels. Our new linearisation is exact, i.e. it does not exclude any orders of scattering, however, it relies on the quality of the Marchenko-derived Green's functions. These Marchenko-based Green's functions require an estimate of the first arrivals of the Green's functions – commonly obtained by modelling in a background medium. Although these first arrival estimates strongly bias our results for inaccurate background models, we find the Marchenko-linearisation to deliver overall slightly better inverted models than the single-scattering approximation.

Key words: Interferometry; Inverse theory; Theoretical seismology; Waveform inversion; Wave propagation.

1 INTRODUCTION

Inferring the physical properties of a volume from its scattering response to incident, e.g. acoustic waves is essential for many applications, ranging from non-destructive testing (Grohmann *et al.* 2017) over medical imaging (Bernard *et al.* 2017; Guasch *et al.* 2020) to seismic imaging (Warner *et al.* 2013). Regarding high-resolution imaging with seismic waves there are two main state-of-the-art strategies in Geophysics: least-squares reverse time migration (LSRTM) and full waveform inversion (FWI). Both of these methods rely on reducing the misfit between the measured, scattering data on the medium's boundary and the respectively estimated data, obtained from numerical modelling.

LSRTM requires a background model, containing the low-wavelength variations of the physical properties and aims to retrieve the missing reflection model, i.e. the short-wavelength model structures that induce scattering (Dai *et al.* 2012). The background model can for instance be obtained via tomography (Rawlinson *et al.* 2010). LSRTM is based on the Born integral (Born & Wolf 1999) which provides an approximate, linear relation between the modelled data and the desired reflection model. This Born integral is at its core a single-scattering approximation, meaning that multiply scattered waves can not be handled accurately in LSRTM (in particular if the unknown, short-wavelength model perturbations are large). There are, however, various strategies to include multiple scattering in LSRTM, dealing with both surface-related multiples (Zuberi & Alkhalifah 2014) and internal multiples (Malcolm *et al.* 2009; Zhang & Schuster 2014; Wang *et al.* 2020).

FWI on the other hand attempts to estimate the model from as little prior information as possible – usually starting with a rather simple initial model (Tarantola 1984; Virieux & Operto 2009; Virieux *et al.* 2017). FWI is a non-linear inversion strategy, i.e. it accurately represents the non-linear relation between modelled data and model. It can be solved in the following way: modelling in the initial model delivers wavefields that can be plugged into the Born integral. This linear system can be solved to obtain an updated model. This new model can then be used for remodelling the wavefields, using Born again and so on. Starting by matching the low-frequency content of the measured data and sequentially including higher frequencies, FWI attempts to avoid artefacts from the single-scattering

© The Author(s) 2023. Published by Oxford University Press on behalf of The Royal Astronomical Society. This is an Open Access article distributed under the terms of the Creative Commons Attribution License (https://creativecommons.org/licenses/by/4.0/), which permits unrestricted reuse, distribution, and reproduction in any medium, provided the original work is properly cited.

Downloaded from https://academic.oup.com/gji/article/234/1/228/7036769 by Centrum voor wiskunde en Informatica user on 05 June 2023

approximation underlying its gradient computations. To further overcome local minima, i.e. converging to wrong models when, e.g. low frequency data is unavailable, improved formulations of FWI, such as extended FWI (Huang *et al.* 2018; van Leeuwen 2019), adaptive waveform inversion (Warner & Guasch 2016) or inversion based on optimal transport (Métivier *et al.* 2019; Engquist & Yang 2022), were presented.

We note that there are also reflection FWI approaches that focus on inverting for high-frequency model perturbations (Yao *et al.* 2020) as well as non-linear formulations of LSRTM (Yao & Jakubowicz 2012). In practice, LSRTM and FWI depart in three main aspects. First, their goal: FWI is generally used as a high-end, long-spatial-scale velocity model building tool, whereas LSRTM aims at retrieving the sharp components – the details – of the subsurface structure, commonly referred to as an image. Secondly, because of their different goals, different parts of the data are employed for FWI (e.g. long-offset data, diving/head waves) and LSRTM (e.g. short-offset data, reflected and diffracted waves) to condition the input data for inversion toward the desired length scales. Thirdly, owing to the different desired scales in target models, FWI and LSRTM often differ on how the models are parametrised in the inverse problem, both in terms of separating background versus update components, as well as physical quantities themselves, e.g. FWI favouring velocity parametrisation and LSRTM favouring impedance or reflectivity parameters. These three key differences often result in significantly different practical strategies in data-misfit metrics, gradient preconditioning/shaping and optimisation.

In this paper, we discuss an alternative to the single-scattering approximation, i.e. another way to obtain a linear relation between the modelled data and the model and thus to compute a model update. Our proposed strategy is fundamentally based on using the Marchenko integral (Wapenaar *et al.* 2014). The Marchenko integral was originally introduced in the context of one-dimensional inverse scattering theory (Burridge 1980; Rose 2001; Broggini *et al.* 2012). It relates Green's functions and so-called focusing functions via the reflection response of the medium measured on its boundary. Its extension to 2D and 3D about 10 yr ago enabled various applications regarding imaging in complex media (Wapenaar *et al.* 2013; Meles *et al.* 2015; Ravasi *et al.* 2016; Vargas *et al.* 2021). Most importantly for this paper, the Marchenko integral allows for retrieving the Green's function for a virtual source inside of an inaccessible medium – it does, however, require an estimate of the first arrival of the desired Green's function. This first arrival is usually obtained by modelling in a smooth background, i.e. a low-wavelength-accurate, medium. This means, that one can obtain the full Green's function, including all orders of scattering, for a virtual source located anywhere inside of the volume of interest without requiring an actual physical source inside the volume or having to know the medium's high-frequency, scattering-inducing physical property perturbations.

Marchenko Green's functions can be used for LSRTM and FWI in various ways. Commonly, the Marchenko method is used for redatuming the wavefields to a target level, where different inversion strategies can be used to image the medium (Cui *et al.* 2020; Shoja *et al.* 2020, 2022). Instead, we propose to use Marchenko-based Green's functions inside the kernel of the inverse problem (Diekmann & Vasconcelos 2020; Diekmann *et al.* 2021): by plugging the estimated Green's functions into the Lippmann–Schwinger integral (Lippmann & Schwinger 1950) we obtain a new, linear relation between modelled data and model. This linear relation can be used to obtain a model update, i.e. to invert for the model. The linearisation is (in theory) exact, i.e. by using the full Green's functions with all orders of scattering rather than background Green's functions (as done in the Born integral) we get an exact, linear system. There are, however, other assumptions and approximations underlying the Marchenko scheme and, consequently, this new linearisation. Hence, we do not necessarily consider this a superior method to well-established schemes, but we aim to explain, discuss and illustrate the possibilities and limitations of using Marchenko methods to linearise seismic imaging. We will refer to our approach as Marchenko-linearised full waveform inversion, although the approach is generally quite similar to LSRTM – it is, however, not based on a single-scattering approximation but supposed to accurately include multiple scattering and therefore the full wavefield.

We start by introducing the Lippmann–Schwinger integral which forms the basis for gradient computations in seismic inversion. Then we discuss Green's function retrieval by the Marchenko method. Next, we discuss our Marchenko-linearised full waveform inversion strategy. Finally we show numerical results for different kernel approximations to compare and evaluate the quality of our new Marchenko-linearisation.

2 LIPPMANN–SCHWINGER INTEGRAL

The constant-density acoustic wave equation is given by

$$\mathcal{L}(\boldsymbol{x},\omega)u(\boldsymbol{x},\omega) = \rho i\omega s(\boldsymbol{x},\omega) \tag{1}$$

with the wave operator

$$\mathcal{L}(\boldsymbol{x},\omega) = \nabla^2 + \frac{\omega^2}{c^2(\boldsymbol{x})}, \tag{2}$$

the wavefield $u(\boldsymbol{x},\omega)$ at location $\boldsymbol{x} = (x_1, x_2, x_3)$ and frequency ω and the volume injection rate density source term $s(\boldsymbol{x},\omega)$. The constant mass density is denoted by ρ and velocity by $c(\boldsymbol{x})$, i marks the imaginary unit.

The Green's function is the causal wavefield that obeys

$$\mathcal{L}(\boldsymbol{x},\omega)g(\boldsymbol{x},\omega;\boldsymbol{x_s}) = \rho i\omega\delta(\boldsymbol{x}-\boldsymbol{x_s}), \tag{3}$$

i.e. it is the medium response to an impulse source at location $\boldsymbol{x_s}$. Similarly, we can define a background Green's function in a background medium, i.e. a medium with different physical properties, for a source at $\boldsymbol{x_r}$ according to

$$\mathcal{L}_0(\boldsymbol{x},\omega)g_0(\boldsymbol{x},\omega;\boldsymbol{x_r}) = \rho i\omega\delta(\boldsymbol{x}-\boldsymbol{x_r}) \tag{4}$$

with

$$\mathcal{L}_0(\boldsymbol{x},\omega) = \nabla^2 + \frac{\omega^2}{c_0^2(\boldsymbol{x})} \tag{5}$$

and the velocity $c_0(\boldsymbol{x})$. We will assume that $c_0(\boldsymbol{x})$ is a smooth background model, while $c(\boldsymbol{x})$ is the actual model. As before, this background Green's function is a causal wavefield.

Using reciprocity (Fokkema & van den Berg 1993; Schuster *et al.* 2009; Snieder & Van Wijk 2015), we can combine eqs (3) and (4) to obtain the following volume integral,

$$g_s(\boldsymbol{x_r},\omega;\boldsymbol{x_s}) = \alpha(\omega)\int_{\boldsymbol{x}\in V} g_0(\boldsymbol{x},\omega;\boldsymbol{x_r})g(\boldsymbol{x},\omega;\boldsymbol{x_s})\nu(\boldsymbol{x})\,\mathrm{d}V, \tag{6}$$

where we use the scattered Green's function

$$g_s(\boldsymbol{x_r},\omega;\boldsymbol{x_s}) = g(\boldsymbol{x_r},\omega;\boldsymbol{x_s}) - g_0(\boldsymbol{x_r},\omega;\boldsymbol{x_s}), \tag{7}$$

the scattering potential

$$\nu(\boldsymbol{x}) = \frac{1}{c^2(\boldsymbol{x})} - \frac{1}{c_0^2(\boldsymbol{x})}, \tag{8}$$

Downloaded from https://academic.oup.com/gji/article/234/1/228/7036769 by Centrum voor wiskunde en Informatica user on 05 June 2023

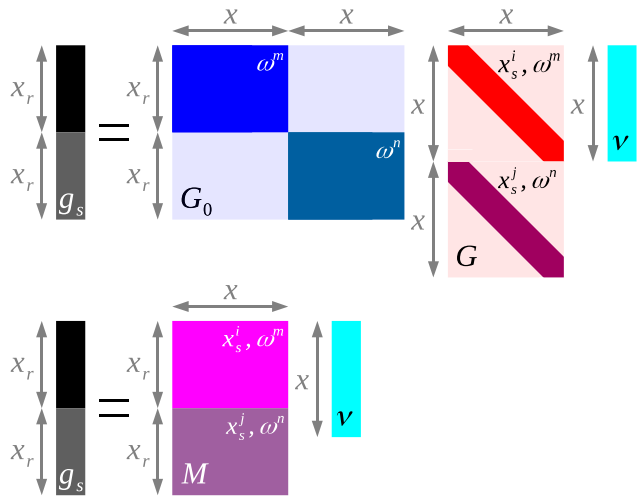

Figure 1. Sketch to illustrate the matrix-operator eqs (10) (top) and (11) (bottom). The matrix **G** (red) is diagonal, whereas $\mathbf{G_0}$ (blue) has dense batches (number of receivers × number of volume sample points) along its diagonal. The matrix **M** (magenta) is dense. The arrows represent which variable, i.e. the receiver location $\boldsymbol{x_r}$ or volume sample $\boldsymbol{x}$, is changing in the respective direction and range. The variables $\boldsymbol{x_s^i}$ and $\boldsymbol{x_s^j}$ and ω^m and ω^n denote different source locations and frequencies, respectively.

and the scaling factor

$$\alpha(\omega) = \frac{i\omega}{\rho}, \tag{9}$$

see Appendix for details. The volume V contains $\boldsymbol{x_r}$ and $\boldsymbol{x_s}$ as well as all perturbations of the scattering potential, i.e. $\nu(\boldsymbol{x} \notin V) = 0$. Eq. (6) is the Lippmann–Schwinger integral (Lippmann & Schwinger 1950).

We can write the Lippmann–Schwinger integral in matrix-operator form as

$$\mathbf{g_s} = \mathbf{G_0 G \nu}, \tag{10}$$

where the matrices $\mathbf{G_0}$ and **G** contain the respective background Green's functions and Green's functions. Note that $\mathbf{G_0}$ also contains the scaling term, see eq. (9), as well as an additional scaling factor to account for the integration, e.g. Δx^2 for a square grid in two dimensions where Δx is the spacial sampling interval. The vector $\mathbf{g_s}$ contains the scattered Green's function, eq. (7) and the vector $\boldsymbol{\nu}$ the scattering potential, eq. (8). Eq. (10) accurately represents a discretized Lippmann–Schwinger integral for multiple receiver locations $\boldsymbol{x_r}$, source locations $\boldsymbol{x_s}$ and frequencies ω; however, it is a fairly big and sparse system; compare Fig. 1. A more convenient way of setting up the linear system is

$$\mathbf{g_s} = \mathbf{M \nu}, \tag{11}$$

where $\mathbf{M} = \mathbf{G_0 G}$ is a dense matrix, see Fig. 1.

3 MARCHENKO-BASED GREEN'S FUNCTION RETRIEVAL

We define the focusing function as the wavefield (Diekmann & Vasconcelos 2021)

$$\mathcal{L}(\boldsymbol{x}, \omega)\big(-f^*(\boldsymbol{x}, \omega; \boldsymbol{x_f})\big) = -\frac{\rho i \omega \delta(\boldsymbol{x} - \boldsymbol{x_f})}{2} - q(\boldsymbol{x}, \omega), \tag{12}$$

where $-f^*(\boldsymbol{x}, \omega; \boldsymbol{x_f})$ obeys a radiation condition of in-coming waves at infinity, i.e. it is an anticausal wavefield and we use the same, non-dissipative wave operator as before, eq. (2). The source term $q(\boldsymbol{x}, \omega)$ has to be real-valued, but is otherwise arbitrary. The symbol $*$ denotes complex conjugation (or time-reversal in the time domain). The negative, conjugate focusing function consequently follows from

$$\mathcal{L}(\boldsymbol{x}, \omega) f(\boldsymbol{x}, \omega; \boldsymbol{x_f}) = -\frac{\rho i \omega \delta(\boldsymbol{x} - \boldsymbol{x_f})}{2} + q(\boldsymbol{x}, \omega). \tag{13}$$

Note that $f(\boldsymbol{x}, \omega; \boldsymbol{x_f})$ is in fact a causal, out-going wavefield. Combining eq. (3) for a source at $\boldsymbol{x_f}$ with eqs (12) and (13) we get the homogeneous Green's function of the second kind (Diekmann *et al.* 2022) as the wavefield that obeys

$$\mathcal{L}(\boldsymbol{x}, \omega)\big(g(\boldsymbol{x}, \omega; \boldsymbol{x_f}) + f(\boldsymbol{x}, \omega; \boldsymbol{x_f}) - f^*(\boldsymbol{x}, \omega; \boldsymbol{x_f})\big) = 0. \tag{14}$$

This is a source-free, i.e. homogeneous, wavefield that relates focusing and Green's functions.

Using reciprocity, we can obtain the following integral equation from the homogeneous Green's function of the second kind,

$$-\int_{\tilde{\boldsymbol{x}} \in \partial V_0} r(\tilde{\boldsymbol{x}}, \omega; \boldsymbol{x_s}) \quad f^*(\tilde{\boldsymbol{x}}, \omega; \boldsymbol{x_f})\, \mathrm{d}\boldsymbol{S} = g(\boldsymbol{x_s}, \omega; \boldsymbol{x_f}) + f(\boldsymbol{x_s}, \omega; \boldsymbol{x_f}), \tag{15}$$

where

$$r(\tilde{\boldsymbol{x}}, \omega; \boldsymbol{x_s}) = -\frac{2}{\rho i \omega} \frac{\partial}{\partial \tilde{x}_3} g(\tilde{\boldsymbol{x}}, \omega; \boldsymbol{x_s}), \tag{16}$$

see Appendix for details. ∂V_0 is a horizontal, open boundary at $x_3 = 0$ bounding the half-space below. Both the focusing location $\boldsymbol{x_f}$ and the source location $\boldsymbol{x_s}$ are in this half-space, but $\boldsymbol{x_s}$ is close to the boundary ∂V_0 (in practice source locations are usually collocated with receivers $\tilde{\boldsymbol{x}}$). Note that eq. (15) only holds true for a very specific type of focusing functions (and thus a specific type of sources $q(\boldsymbol{x}, \omega)$ in eq. (12)), i.e. these wavefields $f(\boldsymbol{x}, \omega; \boldsymbol{x_f})$ only propagate between $\boldsymbol{x_f}$ and ∂V_0 but vanish in other directions of the half-space (Diekmann *et al.* 2022). We refer to this as a radiation assumption because we assume focusing functions with a very particular radiation pattern. Eq. (15) generally relates focusing and Green's functions via the surface reflection data $r(\tilde{\boldsymbol{x}}, \omega; \boldsymbol{x_s})$. In order to use this integral for Green's function retrieval, an additional step is necessary.

Building on experiences in one-dimensional inverse scattering theory, Wapenaar *et al.* (2014) suggested to rewrite eq. (15) to

$$-\Theta(\boldsymbol{x_s}, \omega; \boldsymbol{x_f}) \star \int_{\tilde{\boldsymbol{x}} \in \partial V_0} r(\tilde{\boldsymbol{x}}, \omega; \boldsymbol{x_s}) f^*(\tilde{\boldsymbol{x}}, \omega; \boldsymbol{x_f})\, \mathrm{d}\boldsymbol{S} = g_{first}(\boldsymbol{x_s}, \omega; \boldsymbol{x_f}) + f(\boldsymbol{x_s}, \omega; \boldsymbol{x_f}) \tag{17}$$

with $\Theta(\boldsymbol{x_s}, \omega; \boldsymbol{x_f})$ being a time-symmetric filter in the time domain, a so-called windowing operator, that mutes everything at $|t| > t_{first}(\boldsymbol{x_s}; \boldsymbol{x_f})$, where $t_{first}(\boldsymbol{x_s}; \boldsymbol{x_f})$ is the first arrival travel time for a source at $\boldsymbol{x_f}$ and a receiver at $\boldsymbol{x_s}$. The symbol $\star$ denotes convolution (along the frequency axis). The first arrival of the Green's function is given by $g_{first}(\boldsymbol{x_s}, \omega; \boldsymbol{x_f}) = \Theta(\boldsymbol{x_s}, \omega; \boldsymbol{x_f}) \star g(\boldsymbol{x_s}, \omega; \boldsymbol{x_f})$, i.e. the windowing operator removes everything after the first arrival from the Green's function. Note that we assume that the focusing function $f(\boldsymbol{x_s}, \omega; \boldsymbol{x_f})$ remains unchanged by the windowing operator, meaning that the focusing function is supposed to be zero for $|t| > t_{first}(\boldsymbol{x_s}; \boldsymbol{x_f})$. We refer to this as a time-separability assumption because it means that the focusing function and the Green's function appear separated from each other in time (apart from a small overlap at the first arrival of the Green's function). Eq. (17) is a Marchenko-type integral.

Downloaded from https://academic.oup.com/gji/article/234/1/228/7036769 by Centrum voor wiskunde en Informatica user on 05 June 2023

In matrix-operator form we can write the Marchenko-type equation as

$$-\mathbf{\Theta R f}^{*} = \mathbf{g}_{\mathbf{first}} + \mathbf{f} \tag{18}$$

and eq. (15) as

$$-\mathbf{R f}^{*} = \mathbf{g} + \mathbf{f} \tag{19}$$

where $-\mathbf{f}^{*}$ is the focusing function vector, $\mathbf{g}_{\mathbf{first}}$ is the vector that contains the first arrivals of the Green's functions and $\mathbf{g}$ is the full Green's function vector. The matrix $\mathbf{R}$ comprises the reflection data, eq. (16), as well as a scaling factor for the integration, e.g. multiplication with the spacial sampling interval Δx for a one-dimensional boundary. The matrix $\mathbf{\Theta}$ accounts for the convolution with the windowing operator.

If both the radiation assumption and the time-separability assumption are met such that eq. (18) holds, we can solve eqs (18) and (19) for the full Green's function $\mathbf{g}$ given the boundary data measurement $\mathbf{R}$ and an estimate of $\mathbf{g}_{\mathbf{first}}$ (which also governs the associated first arrival travel times for the construction of the windowing operator $\mathbf{\Theta}$) according to

$$\mathbf{g} = \mathbf{g}_{\mathbf{first}} + \Lambda \mathbf{R}(\mathbf{I} - \mathbf{\Theta R}^{*}\mathbf{\Theta R})^{-1}(\mathbf{g}^{*}_{\mathbf{first}} - \mathbf{\Theta R}^{*}\mathbf{g}_{\mathbf{first}}), \tag{20}$$

where $\mathbf{\Lambda} = \mathbf{I} - \mathbf{\Theta}$, i.e. it mutes all data at $|t| \leq t_{first}(\boldsymbol{x_s}; \boldsymbol{x_f})$ and $\mathbf{I}$ is the identity operator (Diekmann & Vasconcelos 2021). Usually, the estimate of the first arrival Green's function $\mathbf{g}_{\mathbf{first}}$ is obtained by modelling in a background medium, i.e. a smooth approximation of the actual model. We can either solve eq. (20) directly (van der Neut *et al.* 2015a; Revelo *et al.* 2022) or approximate it by a truncated Neumann expansion (van der Neut *et al.* 2015b),

$$\begin{aligned}\mathbf{g} = \mathbf{g}_{\mathbf{first}} &+ \Lambda \mathbf{R}\mathbf{g}^{*}_{\mathbf{first}} - \Lambda \mathbf{R\Theta R}^{*}\mathbf{g}_{\mathbf{first}} \\ &+ \Lambda \mathbf{R\Theta R}^{*}\mathbf{\Theta R}\mathbf{g}^{*}_{\mathbf{first}} - \Lambda \mathbf{R\Theta R}^{*}\mathbf{\Theta R\Theta R}^{*}\mathbf{g}_{\mathbf{first}} + \dots .\end{aligned} \tag{21}$$

For the numerical examples in this paper we use a Neumann expansion that is truncated after the last explicitly given term in eq. (21). This rather early truncation ensures a relatively stable Green's function estimation even if our assumptions about radiation and time-separability (and thus the theoretical justification for the Marchenko-type integral) are not perfectly satisfied. This might for instance happen, when dealing with complicated models or when only a poor estimate of the first arrival Green's function is given.

Finally, we illustrate the capability of Marchenko-based Green's function retrieval in Fig. 2. We compare different Green's function traces for a source inside the volume and a receiver on its surface. We use a slightly modified version of the Marmousi model. Modelling in the true medium delivers various events, see multitude of wiggles, because the wavefield is reflected at the sharp interfaces between different velocity layers, inducing multiple scattering. Modelling in the smooth background medium on the other hand, delivers a very similar first arrival but hardly any multiple scattering. By muting everything after the first arrival of the background Green's function, we obtain an estimate of $\mathbf{g}_{\mathbf{first}}$. Using this estimate along with the consequent window operator $\mathbf{\Theta}$ and the surface data $\mathbf{R}$ in eq. (21) we get the Marchenko-based Green's function. This Green's function is quite similar to the true-model Green's function. Note that we did not need an actual source or receiver inside the true model to obtain this estimate. This demonstrates how we can obtain full Green's functions, i.e. including all orders of scattering, for virtual sources inside of an inaccessible volume from a smooth background model and surface scattering data.

4 SOLVING THE MARCHENKO-LINEARISED LIPPMANN–SCHWINGER INTEGRAL FOR THE SCATTERING POTENTIAL

To this point, we introduced the Lippmann–Schwinger integral and the Marchenko-type integral. In this section, we present the concept of Marchenko-linearised full waveform inversion by sequentially making use of both integrals. We want to stress right away that although we refer to the following procedure as FWI, it is quite similar to LSRTM as well. We will discuss this ambiguity at the end of the section.Using a Tikhonov regularisation with $\beta \in R^{+}$ we can estimate the real-valued scattering potential $\boldsymbol{\nu}$ from eq. (11) by minimising the objective function

$$s(\boldsymbol{\nu}; \beta) = \left\|\mathbf{M}\boldsymbol{\nu} - \mathbf{g_s}\right\|_2^2 + \beta\left\|\boldsymbol{\nu}\right\|_2^2 . \tag{22}$$

The first term is the residual norm, the second term the solution norm. Note that for our example the scattering potential is given by eq. (8) and indeed real-valued. While this does not necessarily imply a real-valued velocity $c(\boldsymbol{x})$ and therefore a physically reasonable result, it is easy to implement and significantly reduces the model space. The matrix $\mathbf{M}$ denotes the kernel, $\mathbf{g_s}$ the data, i.e. it comes from a measurement. Hence, the objective function depends on the unknown scattering potential $\boldsymbol{\nu}$ as well as the regularisation value β. We minimise $s(\boldsymbol{\nu}, \beta)$ for a given β by solving the following linear system:

$$\underbrace{\begin{bmatrix} \Re(\mathbf{M}) \\ \Im(\mathbf{M}) \\ \sqrt{\beta}\mathbf{I} \end{bmatrix}}_{\mathbf{Q}} \boldsymbol{\nu} = \underbrace{\begin{bmatrix} \Re(\mathbf{g_s}) \\ \Im(\mathbf{g_s}) \\ \mathbf{0} \end{bmatrix}}_{\mathbf{d}} , \tag{23}$$

where $\Re(\mathbf{M})$ and $\Im(\mathbf{M})$ are the real and imaginary parts of the matrix $\mathbf{M}$, respectively and $\mathbf{0}$ is a vector full of zeros. The explicit solution consequently is

$$\boldsymbol{\nu} = (\mathbf{Q}^{\dagger}\mathbf{Q})^{-1}(\mathbf{Q}^{\dagger}\mathbf{d}), \tag{24}$$

where $\dagger$ generally denotes the adjoint but in this case simplifies to the transpose as $\mathbf{Q}$ is real-valued. Since $\mathbf{Q}$ easily becomes very large when looking at multiple sources, receivers and frequencies, we do not explicitly build this matrix. Instead, we use a matrix-free approach to solve eq. (23) via LSQR (Paige & Saunders 1982). We do, however, use a great number of iterations in LSQR to make sure that we converge (within some pre-defined tolerance) to the actual solution in eq. (24) if possible.

Apart from the size of the inverse problem, we also have to deal with its non-linearity. In fact, the kernel matrix $\mathbf{M} = \mathbf{G_0 G}$ used in $\mathbf{Q}$ is usually unknown. This is because we do not have any measurements of the Green's function $\mathbf{G}$ within the volume but only at its surface. Note that we do know $\mathbf{G_0}$, i.e. we use modelling in a background model (usually a smooth, tomographic approximation of the actual model) to obtain it.

Conventionally, $\mathbf{G}$ is approximated by $\mathbf{G_0}$ under the assumption that $\boldsymbol{\nu}$ is small, leading the kernel $\mathbf{M} \approx \mathbf{G_0 G_0}$. This is called the single-scattering approximation, i.e. this kernel is generally able to reproduce primary reflections but all higher order scattering is neglected. This kernel is also at the core of the Born approximation (Born & Wolf 1999). The Born approximation, however, involves an additional linearisation in order to, e.g. directly invert for the velocity perturbation $c(\boldsymbol{x}) - c_0(\boldsymbol{x})$ rather than the scattering potential $\nu(\boldsymbol{x})$.

We propose an alternative to the single-scattering approximation. Using the same, smooth background model, that we would use for

Downloaded from https://academic.oup.com/gji/article/234/1/228/7036769 by Centrum voor wiskunde en Informatica user on 05 June 2023

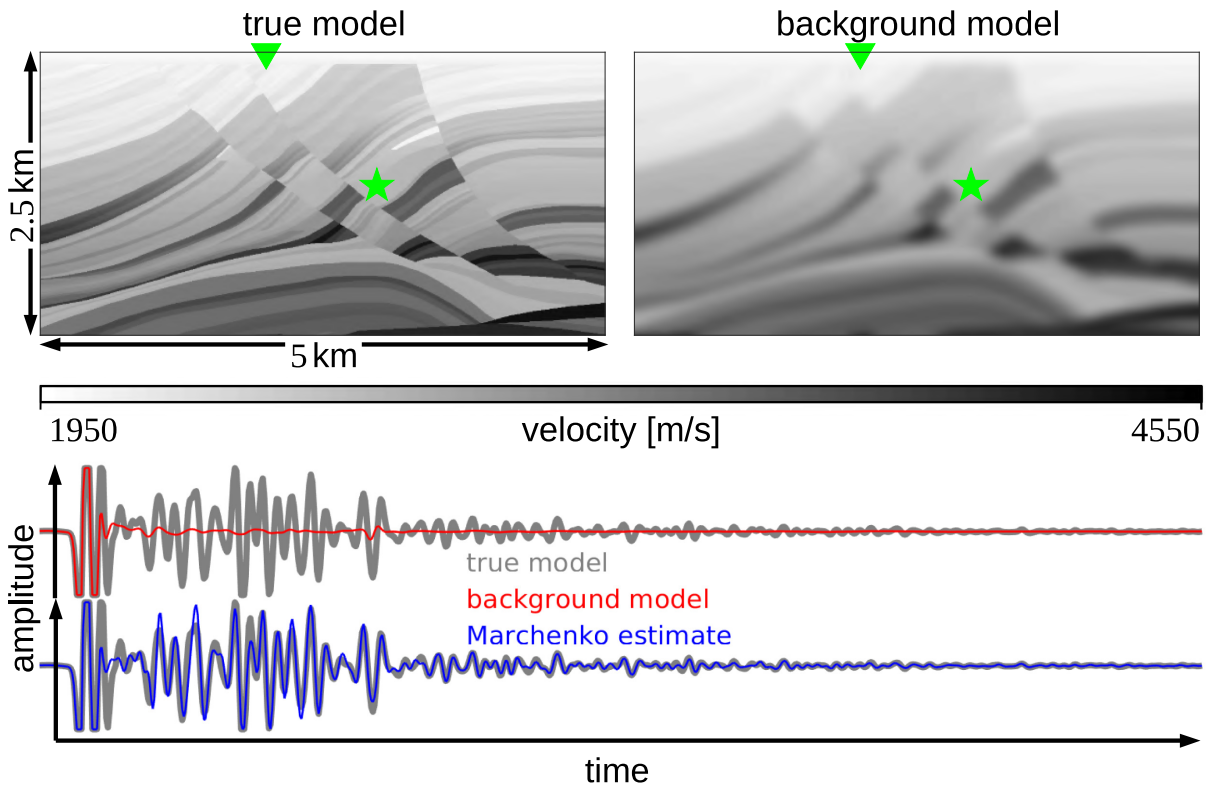

Figure 2. True Marmousi model (top left) and smooth background model (top right). Comparison of different Green's functions (bottom): the grey line is the Green's function modelled in the true medium (top left), the red line is the one modelled in the background medium (top right) and the blue one is obtained by using the background medium (top right) in a Marchenko-based Green's function retrieval scheme. All Green's functions are for a source inside the volume (green star) and a receiver at the surface (green triangle). Note that amplitudes at later arrival times are consistently magnified to allow for a good comparison.

the single-scattering approximation, in a Marchenko-based Green's function retrieval scheme we are able to obtain full, i.e. including all orders of scattering, Green's functions $g(\boldsymbol{x_s}, \omega; \boldsymbol{x_f})$ – for sources $\boldsymbol{x_f}$ anywhere inside the volume and receivers $\boldsymbol{x_s}$ on the boundary ∂V_0. By actually stepping through the entire discretised volume, i.e. solving for all $\boldsymbol{x_f}$ within some bounds, we are able to obtain an estimate of the matrix $\mathbf{G}$ by source-receiver reciprocity, i.e. we get $g(\boldsymbol{x_f}, \omega; \boldsymbol{x_s})$ for all $\boldsymbol{x_f} \in V$. Obviously, it is an important question how to discretise the volume: with a fine grid the amount of Green's functions that need to be estimated is very high, whereas a coarse grid comes with significantly fewer Green's function estimations but also sets limits to the achievable inversion accuracy in terms of wave number. We will refer to this Marchenko-based Green's function matrix as $\mathbf{G_0^M}$. It allows for the kernel approximation $\mathbf{M} \approx \mathbf{G_0}\mathbf{G_0^M}$ which we will call the Marchenko approximation. Although we call it an approximation it is important to note that $\mathbf{G_0^M}$ contains all orders of scattering and is, as we have shown visually in Fig. 2, very similar to $\mathbf{G}$ even when the respective $\mathbf{G_0}$, i.e. the Green's function which is modelled in the same background model that we use for Marchenko, is not. In that sense, this kernel appears to represent the physics significantly better and we are hoping to achieve improved inversion results for $\boldsymbol{\nu}$ in terms of reduced artefacts and increased resolution (Diekmann & Vasconcelos 2020). Note, however, that $\mathbf{G_0^M}$ remains an approximation due to the impact of the first arrival Green's function, which is conventionally approximated by modelling in a background medium, as well as the Marchenko scheme, i.e. the potentially approximate procedure of solving the inverse in eq. (20). Additionally, there might be a bias from the Marchenko-type equation itself when the radiation assumption or the time-separability assumption is broken.

Because we want to have a sort of reference kernel for both the single-scattering and the Marchenko approximation we also introduce the wavefields $\mathbf{G^F}$ and $\mathbf{G^M}$. The Green's functions $\mathbf{G^F}$ are obtained from the actual Green's functions, i.e. modelled in the true medium, by muting everything that arrives after the respective first arrivals. Hence, only the very first event of each Green's function remains. From this we can construct the single-scattering reference kernel $\mathbf{M} \approx \mathbf{G_0}\mathbf{G^F}$. Note that this is not a representation of what actually happens within the single-scattering framework when $\boldsymbol{\nu}$ goes to zero. Instead, we want to use this reference kernel to distinguish between the effects of missing higher order scattering versus having a wrong background model. The matrix $\mathbf{G^M}$ is the Marchenko-based estimate that uses the first arrival of the actual Green's function, i.e. $\mathbf{G^F}$, rather than the first arrival of the background Green's function. Thus, we can build the Marchenko reference kernel $\mathbf{M} \approx \mathbf{G_0}\mathbf{G^M}$.

Table 1 gives a quick overview of the different Green's function matrices, while Table 2 summarises the different kernels and their names.

Fig. 3 shows exemplary Green's function snapshots for the different scenarios discussed above. The Green's function approximations that use the background model, i.e. $\mathbf{G_0}$ and $\mathbf{G_0^M}$, exhibit a distinct error around the first arrival. This is because they are based on a different velocity model, implying different travel times and amplitudes. $\mathbf{G_0^M}$ does, however, recover most of the multiple scattering. The approximations based on the true model on the other hand, i.e. $\mathbf{G^F}$ and $\mathbf{G^M}$, match the first arrival of the true Green's function. The

Downloaded from https://academic.oup.com/gji/article/234/1/228/7036769 by Centrum voor wiskunde en Informatica user on 05 June 2023

Table 1. Overview of different Green's function matrices.

Matrix	Meaning
$\mathbf{G}$	Green's function in true model
$\mathbf{G_0}$	Green's function in background model
$\mathbf{G_0^M}$	Marchenko-reconstructed Green's function using first arrival in background model
$\mathbf{G^F}$	First arrival of Green's function in true model
$\mathbf{G^M}$	Marchenko-reconstructed Green's function using first arrival in true model

Table 2. Different inversion kernels and their names.

Kernel	Name
$\mathbf{G_0G}$	Reference
$\mathbf{G_0G_0}$	Single-scattering
$\mathbf{G_0G_0^M}$	Marchenko
$\mathbf{G_0G^F}$	Single-scattering reference
$\mathbf{G_0G^M}$	Marchenko reference

Marchenko estimate $\mathbf{G^M}$ indeed recovers nearly the entire Green's function with only small errors.

Fig. 4 shows the frequency spectrum of the source wavelet along with an exemplary reference kernel and the misfits of the respective kernel approximations. All fields are in the frequency domain at 20 Hz. The intricate scattering behaviour of the medium leads to complicated interference patterns within the kernel. As expected, the background-based kernel approximations, i.e. the single-scattering and the Marchenko kernel, exhibit overall larger misfits than the true-model-based approximations, i.e. the single-scattering reference and the Marchenko reference kernel. The Marchenko results, however, are superior to the respective single-scattering results in both cases: the Marchenko kernel matches the reference kernel significantly better in the top central part of the model compared to the single-scattering kernel (see black ellipses) and the Marchenko reference kernel is a close to perfect match in the central model area whereas the single-scattering reference kernel is not (see black rectangles).

We introduced two different ways to linearise the inverse problem of solving eq. (23) for $\boldsymbol{\nu}$ based on a background model: the single-scattering approximation and the Marchenko approximation. The process of using the single-scattering approximation to solve eq. (23) is conventionally referred to as least-squares reverse time migration. This is a linear inverse problem and requires a relatively accurate background model. Full waveform inversion, on the other hand, is based on non-linear inversion. It is similar to reverse time migration in that it uses a single-scattering approximation to obtain model updates. However, FWI is an iterative process: it starts with $\mathbf{G_0}$ from some initial background model and computes a model update based on the single-scattering approximation. Then, the wavefield $\mathbf{G_0}$ is remodelled in the new, updated medium. From this new $\mathbf{G_0}$ one gets a new model update and so on. In that sense, FWI uses wave-equation modelling and is not solely build on Born modelling, i.e. the single-scattering approximation. In the light of these differences we call our proposed Marchenko-linearised inversion a full waveform inversion strategy because it is not based on a single-scattering approximation or Born modelling. It is, however, a linear inversion strategy and its outcome is a scattering potential, i.e. a perturbation with respect to the background model, rather than a model. We note that our approach can also be used for gradient

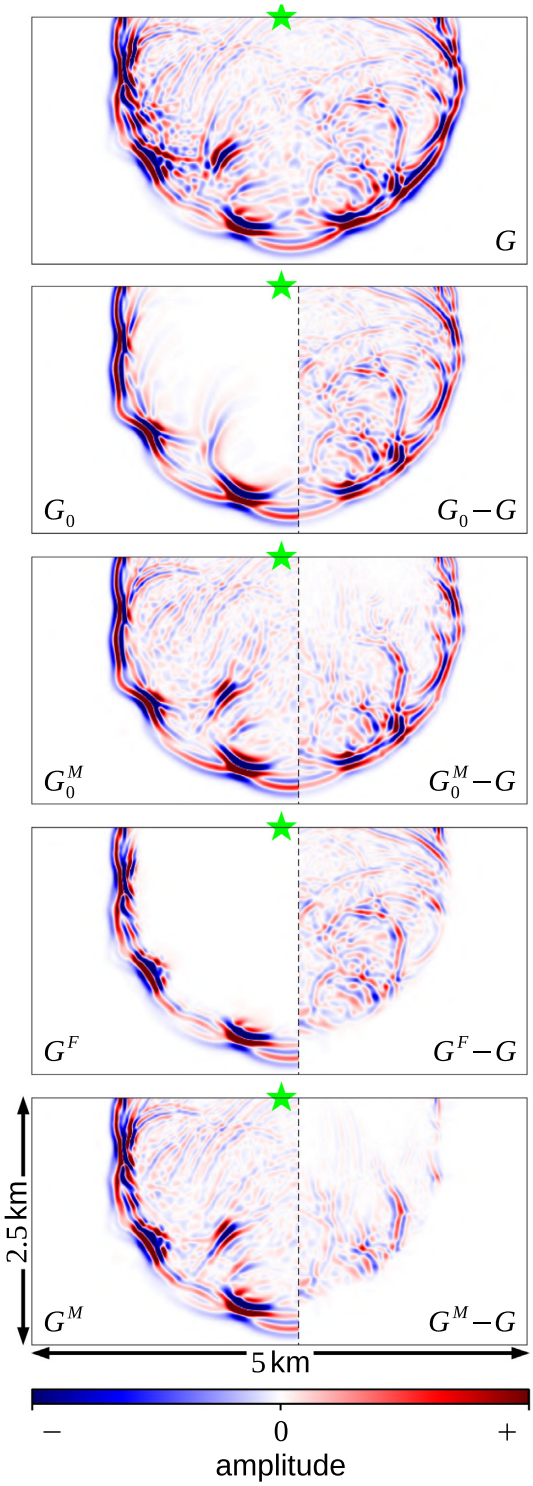

Figure 3. Examples of snapshots at 0.8 s for different Green's functions using the true model and the background model as shown in Fig. 2. The names are analogous to Table 1. For the four approximations (second panel to last panel) of $\mathbf{G}$ (first panel) the left parts of the panels shows the actual fields, whereas the right parts show the differences. The green stars denote the source location. All fields (Green's functions and wavefield differences) are clipped at the same values for a direct comparison. Note that these clip values are relatively small to enhance the visibility of multiple scattering and wavefield differences.

Downloaded from https://academic.oup.com/gji/article/234/1/228/7036769 by Centrum voor wiskunde en Informatica user on 05 June 2023

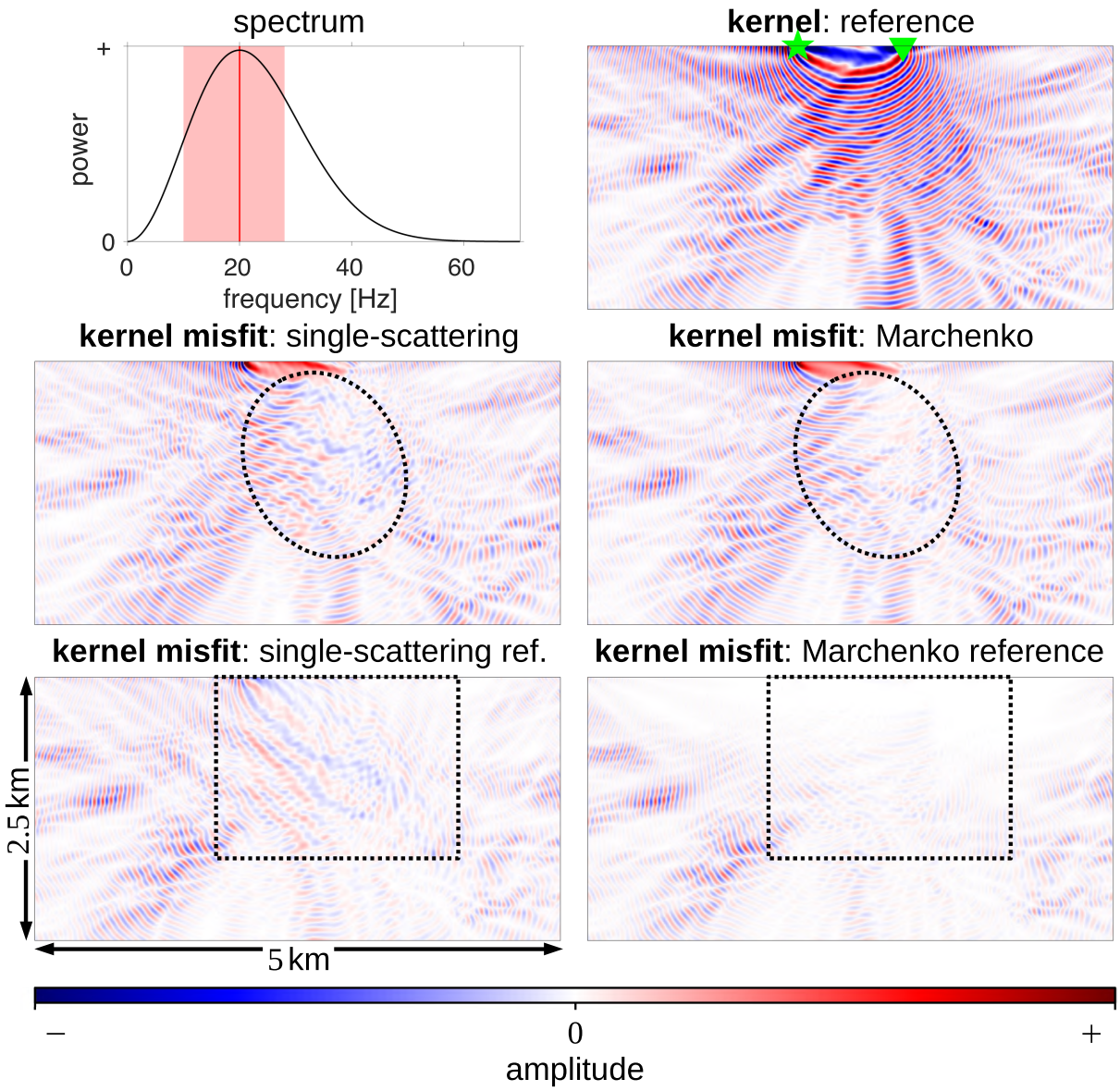

Figure 4. Top left: frequency spectrum of the source wavelet (20 Hz Ricker). The red area denotes the frequencies used for inversion, the red line marks 20 Hz, i.e. the frequency for which we analyse the kernels. Real part of the reference kernel (top right). Source and receiver are denoted by the green star and the green triangle, respectively. Real parts of the kernel misfits (lower four panels) for the single-scattering, Marchenko, single-scattering reference and Marchenko reference approximations. All kernels are based on the models in Fig. 2, kernel names are analogous to Table 2. Kernel and kernel misfits are clipped at the same values for a direct comparison. Hence, white colour in a kernel misfit indicates a good approximation. Dashed, black ellipses and rectangles outline areas that are compared in the text.

computations only, i.e. it can be incorporated in a non-linear FWI strategy.

5 NUMERICAL EXAMPLES

In this section we show and discuss inversion results for the different kernels in Table 2 and various background models, see Fig. 5. The true model is shown in Fig. 1. The model space is discretised with an interval step of 5m in both directions, i.e. x_1 and x_3. We use a 20-Hz Ricker wavelet, see Fig. 4, for forward modelling wavefields. The Marchenko-based Green's functions are estimated with a truncated Neumann expansion according to eq. (21). To save computation time we estimate these Green's functions on a coarse grid, i.e. with a 20 m increment, covering the same 2.5 km × 5 km volume. For the inversions we use 25 frequencies from 10 to 28 Hz with a sampling interval of 0.75 Hz, see again Fig. 4. The upper limit of 28 Hz is related to the coarse spatial grid on which we estimate the Marchenko-based Green's functions. Assuming a minimum medium velocity of 2000 m s^{-1} and a maximum frequency of 28 Hz we get a minimum wavelength of about 71 m. Such a wavefield is therefore sampled more than 2.5 times (in the diagonal grid direction) per wavelength on the coarse grid, allowing for an accurate computation of the volume integral, see eq. (6), in the inversion. Including higher frequencies in the inversions would require estimating the Green's functions on a finer grid. For the inversions we use 126 sources and 125 receivers, all located on the surface of the volume ($x_3 = 0$, i.e. the top boundary) and equally distributed over

Downloaded from https://academic.oup.com/gji/article/234/1/228/7036769 by Centrum voor wiskunde en Informatica user on 05 June 2023

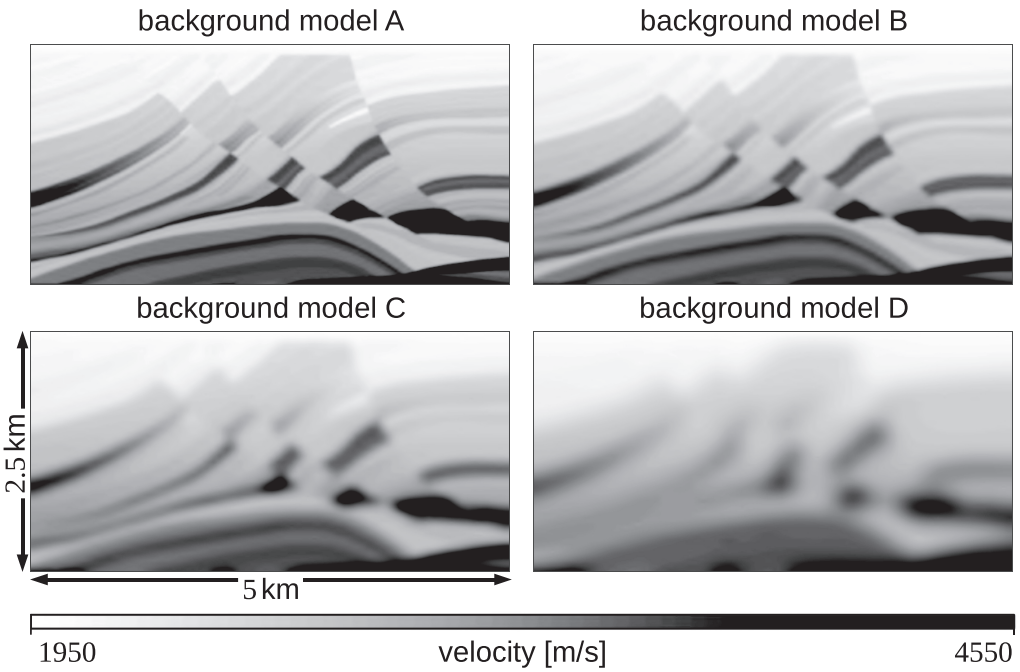

Figure 5. Four different background models with increasing smoothness from model A to model D. Background model C is the same as the background model in Fig. 2.

the 5 km model range. Hence, we have a source at 0 m, a receiver at 20 m, a source at 40 m, a receiver at 60 m and so on. We solve for the respective scattering potentials via LSQR with a tolerance of 10^{-4} and a maximum of 250 iterations for all sources, receivers and frequencies simultaneously. As indicated before, we use LSQR with a MATLAB function handle rather than explicitly defining the matrix $\mathbf{M}$ in eq. (11) – for double-precision variables in our scenario this matrix $\mathbf{M}$ would consume nearly 200 GB of memory.

In order to analyse the quality of different inversion strategies, i.e. for various kernels and background models, we propose to look at the L-curves in Fig. 6. An L-curve is obtained by solving eq. (24) for different values of β (the kernel $\mathbf{M}$ and data $\mathbf{g}_s$ are fixed of course). Conventionally, an L-curve is used to determine the optimal regularisation value β. However, it also carries information on the general behaviour of the respective inverse problem, i.e. on how ill- or well-posed it is. Note that we use LSQR to mimic the L-curves, i.e. our L-curves will be less divergent for small regularisation values. We stress that we use noise-free data. However, all the kernels that we investigate (with the exception of the reference kernel) are approximative and we investigate their L-curves as a measure of how ill- or well-posed the respective inverse problems become.

For instance, we find that at large regularisation values β the type of kernel used in our inversion does not matter very much: all kernels lead similar results for a large value of β and this is true for all background models, see Fig. 6. Note that we do not actually look at the inverted scattering potentials here but only at the respective residual norms and solution norms. Hence, coinciding L-curves do not imply identical models, however, they imply models of similar quality (as measured by our objective function). We stress here that this quality comparison is not perfectly accurate because we are using different kernels, i.e. the residual norms are computed in different ways.

As we go to lower regularisation values, we observe different results depending on the kernel and background model. For all background models, the reference kernel performs much better than any of the four approximated kernels. Even for low regularisation values it delivers reasonable results with relatively small solution norms. This means that we require a small regularisation for the inverse problem using the reference kernel because it accurately represents the physics that governed the data, while we need a high regularisation for, e.g. the single-scattering kernel which is inconsistent with the physics underlying the data.

For a bad background model, i.e. a smooth estimate similar to model D, we observe that the single-scattering and the Marchenko kernel lead to similar results. The single-scattering reference kernel delivers a much better L-curve, but the Marchenko reference kernel is clearly the best approximation. We can interpret this as follows: using the Marchenko-based Green's functions from a smooth background model does not lead to a significantly improved kernel compared to the conventional single-scattering kernel – at least in terms of model quality. Even though the Marchenko kernel contains all orders of scattering, it is fundamentally relying on the background model: travel times and amplitudes are therefore not accurate enough to enable a beneficial linearisation of the Lippmann–Schwinger integral. This limitation is, however, primarily related to our prior knowledge (the background model), not to the Marchenko scheme itself. This can be seen by the good Marchenko reference result. While it is not perfect (due to, e.g. the limited measurement aperture and the early truncation of the Neumann series) it apparently represents a fairly good approximation – even for such a complicated model as Marmousi. Note that the single-scattering reference kernel is not as successful, i.e. the Marchenko-based retrieval of multiply scattered events in the Green's functions is essential.

For a good background model, i.e. an estimate that is close to the true model (like background model A), the four approximated kernels generally perform comparably well. The single-scattering reference kernel is slightly worse, missing multiple scattering that

Downloaded from https://academic.oup.com/gji/article/234/1/228/7036769 by Centrum voor wiskunde en Informatica user on 05 June 2023

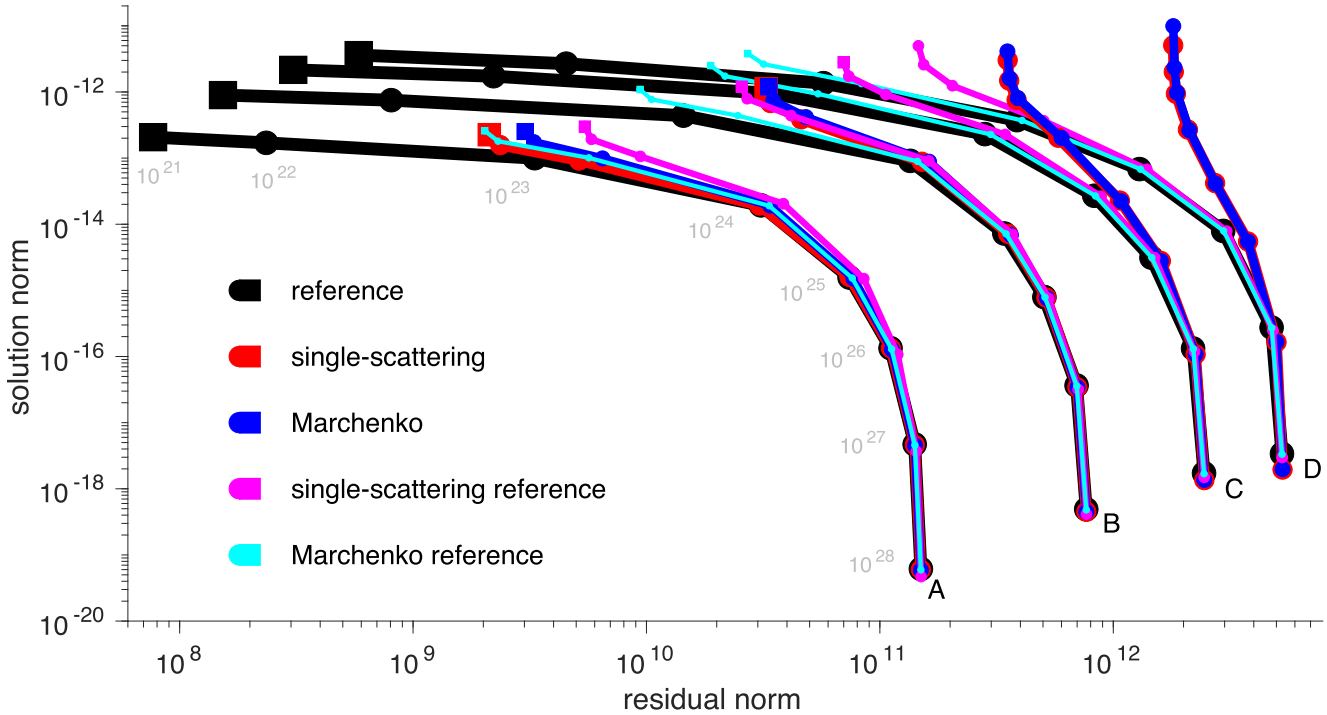

Figure 6. L-curves for the four different background models (A, B, C and D from sharpest to smoothest as shown in Fig. 5) and the five different inversion kernels, see Table 2. While kernels can be differentiated by colour, the different background models are marked in the vicinity of the respective first, i.e. highest regularisation value β in eq. (22), sample point of each line in the bottom right corner. Note that all L-curves for different kernels start out in the same region for the same background model, but diverge for decreasing regularisation values β towards the top left corner. We use the same eight regularisation values β (from 10^{28} to 10^{21}) to sample all L-curves. Exemplarily, the different β sample points are written into the plot for the lowermost black curve. The residual norm is the first term and the solution norm the second term (without the factor β) in eq. (22). Circles denote convergent (for the tolerance and maximum number of iterations as described in the text), squares denote non-convergent inversion runs – the latter only occur for some of the experiments and only for the lowermost regularisation value β. Note that the solution norm is related to a summation over $(c^{-2}(\boldsymbol{x}) - c_0^{-2}(\boldsymbol{x}))^2$ for all $\boldsymbol{x}$ such that its small values are due to the velocity unit being m/s here.

is included in the Marchenko kernels and, for a sharp background model, even in the single-scattering kernel.

Fig. 7 shows inverted scattering potentials for background model C and $\beta = 10^{22}$, i.e. the penultimate β value. The reference result is quite close to the true potential. It is, however, significantly smoother. This is because we solve for the scattering potentials on the coarse grid (20 m sampling interval). Given the L-curve, see Fig. 6, it seems as if going to even smaller β values (beyond our last sample point at $\beta = 10^{21}$) might further push the quality of the inverted scattering potential for the reference kernel. Both the single-scattering and the Marchenko result contain a significant amount of artefacts. The Marchenko result contains high-frequency noise near the surface that is not present in the single-scattering result, see magenta box A for strongest artefacts in Figs 7 and 8. These are potentially related to the unphysical combination of the background-model-consistent arrival times/amplitudes and the Marchenko-recovered multiple scattering – ultimately this leads a Green's function in the Marchenko kernel that is neither consistent with the true model nor with the background model. On the other hand, it seems that the Marchenko result is slightly better in several areas of the model, see cyan boxes in Fig. 7. For zoomed versions of the boxes see Fig. 8. Several interfaces appear to be disrupted in the single-scattering solution while they are continuous in the Marchenko and the reference result. When comparing the single-scattering reference and the Marchenko reference result, we observe that the latter is close to perfect, i.e. it is very similar to the reference solution, while the single-scattering reference solution is still prone to artefacts.

Fig. 9 shows scattering potentials for background model B. As before, we present the true potential and the results for the five kernels in Table 2 for $\beta = 10^{22}$. Owing to the sharper background model, the scattering potential is overall lower than in the previous example. The general observations, however, are the same. There are still some high-frequency artefacts in the Marchenko solution, but they are less distinct than before, see box A. The Marchenko result is slightly better than the single-scattering result, see boxes B, C and D in Figs 9 and 10. The Marchenko reference result is a nearly perfect match of the reference potential and better than the single-scattering reference.

These examples demonstrate that even though the single-scattering kernel and the Marchenko kernel deliver similar-quality results in terms of residual norms and solution norms in Fig. 6, the actual scattering potentials are different: the Marchenko kernel is slightly superior in recovering the medium structures particularly in the central model area, but it is biased by high-frequency noise. As pointed out before, the main issue of the Marchenko kernel is the inherent dependency on the background model: as we do not update the first arrival Green's function in the Marchenko scheme, eq. (20), the final Marchenko-based Green's function becomes a sort of hybrid of the background and the true Green's function. The Marchenko reference kernel on the other hand delivers a nearly perfect result and performs significantly better than

Downloaded from https://academic.oup.com/gji/article/234/1/228/7036769 by Centrum voor wiskunde en Informatica user on 05 June 2023

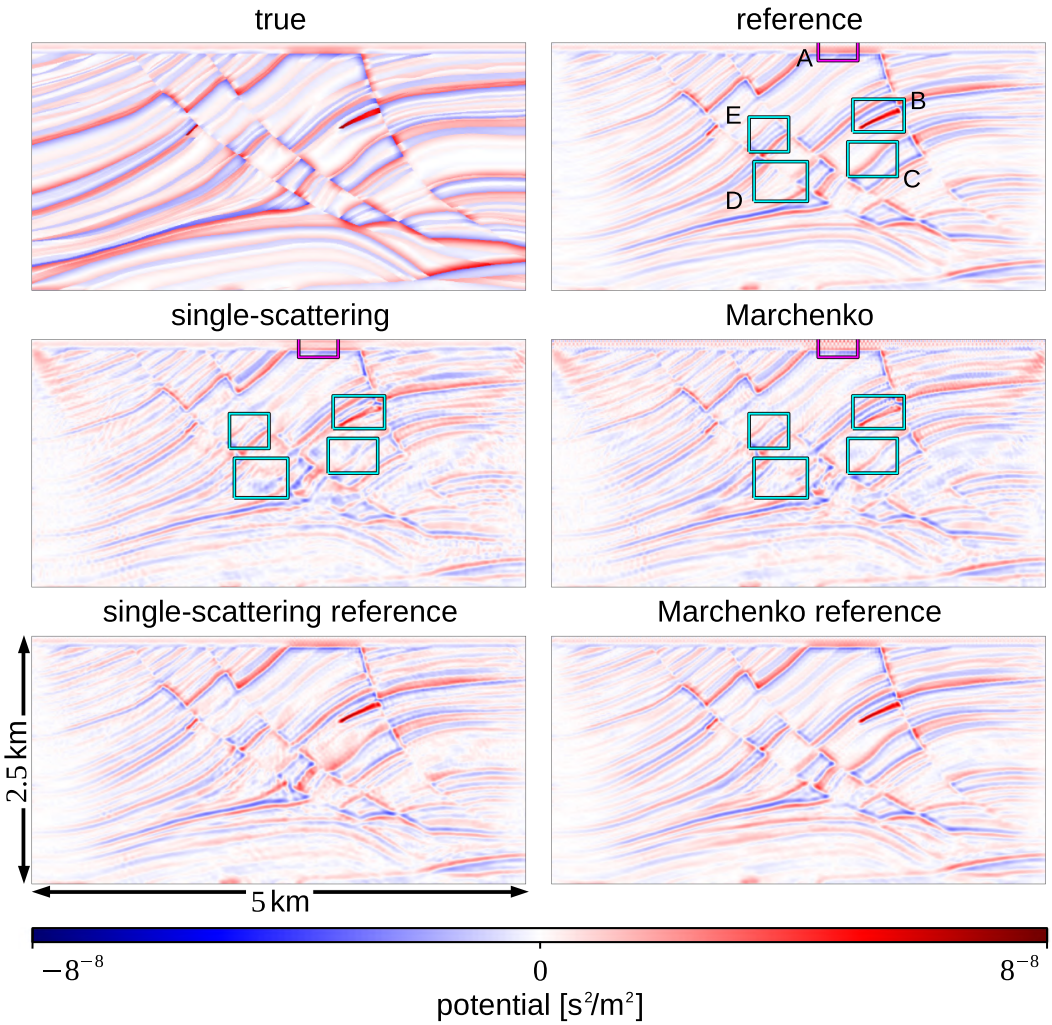

Figure 7. Scattering potentials for the true model in Fig. 2 and background model C, Fig. 5. The true potential (top left) follows from eq. (8). The five inverted potentials are for the different kernels in Table 2. All inversion results are for a regularisation parameter $\beta = 10^{22}$. The magenta box denotes artefacts in the Marchenko solution. Cyan boxes denote areas where the Marchenko result is better than the single-scattering result. See Fig. 8 for zoomed boxes.

the single-scattering reference kernel – hence, including multiple scattering in the kernel generally adds considerably to the quality of the inverted potential.

6 DISCUSSION

We introduced an approach for Marchenko-linearised full waveform inversion. We refer to the method as full waveform inversion rather than least-squares migration because it is not based on a single-scattering approximation. Instead, the linearisation of the inverse problem is based on replacing the unknown Green's functions inside the Lippmann–Schwinger integral by Marchenko-based Green's functions. These Marchenko-based Green's functions contain all orders of scattering. They require reflection data on the surface and an estimate of the first arrival of the Green's function, e.g. from modelling in a background medium – they do, however, not rely on sharp medium contrasts in the background model to induce the scattered waves. The quality of the Marchenko-based Green's functions appears to be quite good, see Fig. 3 and the respective Marchenko kernel is a better approximation than the single-scattering kernel, see Fig. 4.

The numerical examples show that the Marchenko kernel tends to deliver a slightly better scattering potential than the single-scattering approximation when comparing the inverted results, but the kernels generally deliver models of similar quality, see L-curves in Fig. 6. The good quality of the Marchenko reference solution indicates that the errors in the Marchenko result are not due to the underlying Marchenko scheme, but due to the prior information on the first arrival of the Green's function. Using a smooth background model inevitably leads to a wrong first arrival of the Green's function in terms of arrival times and amplitudes – an error that is currently not compensated for in the Marchenko scheme. These errors lead to a Marchenko-based Green's function that includes multiple scattering (as if being related to a sharp model) but that is also consistent with the smooth background model in terms of the first arrival. Note that the Marchenko kernel $\mathbf{G_0 G_0^M}$ is an approximation due to the underlying background model, while the Marchenko reference kernel $\mathbf{G_0 G^M}$ is exact if all underlying assumptions (regarding, e.g. the radiation and time-separability of focusing functions in the Marchenko scheme) are met. Including multiples in the kernel generally leads to better results – this is also true when comparing the Marchenko reference and the single-scattering reference solutions.

Downloaded from https://academic.oup.com/gji/article/234/1/228/7036769 by Centrum voor wiskunde en Informatica user on 05 June 2023

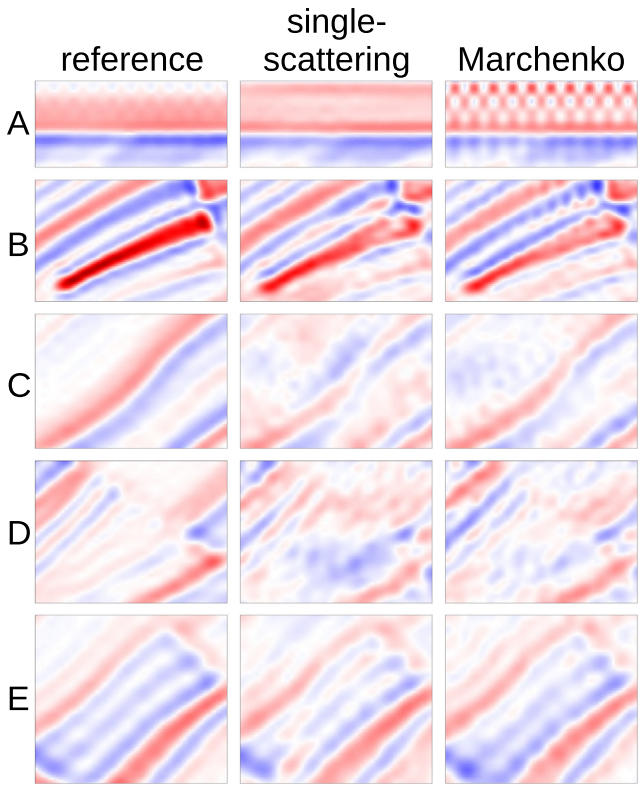

Figure 8. Zoomed versions of the highlighted areas in Fig. 7. The letters A, B, C, D and E refer to the different boxes, see Fig. 7. We show these zoomed images for the reference kernel, the single-scattering kernel and the Marchenko kernel, see Table 2.

Broggini *et al.* (2014) used Marchenko-derived Green's functions for imaging via multidimensional deconvolution. This approach appears to have the benefit of suppressing artefacts from first arrival Green's function errors by further relying on the data domain rather than going to the model domain and using a wave equation, as done in our study. The fact that Marchenko-linearised full waveform inversion is strongly depending on the first arrival estimate of the Green's function makes it hard to exploit the full potential of Marchenko-based Green's function retrieval. For strongly scattering, high-impedance media we would expect Marchenko-based imaging to be significantly superior to Born-based approaches. These media, however, usually imply larger errors in the first arrival Green's functions due to, e.g. modelling in a background model that smooths over strong contrasts in the true medium and are consequently hard to image via Marchenko-linearised full waveform inversion.

We do not argue that our Marchenko-linearised full waveform inversion is in any way better than full waveform inversion or least-squares reverse time migration. The aim of this paper is first and foremost to study and illustrate the possibilities and limits of such a Marchenko-linearisation. We showed how the Marchenko method can be connected to conventional imaging workflows like FWI and LSRTM and hope that this might pave the way for future imaging techniques. The current Marchenko-linearised inversion workflow is computationally expensive. This is, as indicated earlier, because we wanted to compare different inversion kernels under optimal circumstances. One might of course develop more elaborate schemes. We used an early truncation of the Neumann series to approximate the Green's functions via eq. (21). This generally leads to relatively stable results and saves a significant amount of computation time as these Green's functions have to be estimated for all points in the volume. However, this early truncation might, especially for a good background model, not deliver the optimal Green's function estimate. Hence, further optimising our approach may not only make it computationally cheaper but also more accurate. This could allow for iterating the process we described, i.e. get new Marchenko-based Green's functions using the inverted velocities as a background model and invert for a new, updated model - similar to (non-linear) full waveform inversion.

Generally, it seems that a parallel approach of combining the Marchenko scheme and full waveform inversion might indeed be desirable. Currently, we combine them in a sequential fashion: first we solve for the Marchenko-based Green's functions, then we invert for the scattering potential. This comes with the issue of the Marchenko-based Green's functions being physically inconsistent (containing features of both the background and the sharp, scattering model). As we saw in this study, the Marchenko equation itself generally performs quite well even for a complicated model like Marmousi, see good inversion results for Marchenko reference kernels in Figs 7 and 9. If we could solve both problems simultaneously we might therefore further benefit from the constraining quality of the Marchenko equation in full waveform inversion.

In this study we assumed to have unknown velocities and, for simplicity, a constant density. However, the density could in fact be arbitrarily heterogeneous in our scheme as long as it is known. Our Marchenko-linearised full waveform inversion might also be interesting in the opposite scenario, i.e. for known velocity and unknown density. Actually, this would imply better knowledge of the first arrival of the Green's function since we would only expect amplitude errors but have correct arrival times. Hence, the Marchenko kernel might perform even better when inverting for density than it did in the examples we presented in this paper, potentially leading to less artefacts and better resolution.

In general, Marchenko-based Green's function retrieval also allows for the following strategy: rather than using the retrieved Green's functions solely in the kernel, i.e. to linearise the inverse problem as discussed above, we can use them as additional data. In particular this means that we can put virtual receivers at every grid point of the volume under investigation. If we have a single source and a single frequency but we have receivers covering the entire volume, eq. (24) actually becomes exact – assuming that we know the Green's function perfectly, that we sample the volume at a sufficiently fine grid with respect to the investigated frequencies and that there are no scattering perturbations outside the volume (Diekmann & Vasconcelos 2020). Or one could use the wave equation to directly invert for the medium properties, similar to seismic gradiometry (De Ridder & Curtis 2017). An exact inverse problem implies that we can retrieve the model with perfect resolution and accuracy. If, however, we use a coarse grid or the Green's functions are slightly biased, the result will be distorted by artefacts. As we discussed earlier, the accuracy of Marchenko-based Green's functions is inherently limited by the prior knowledge of the first arrival Green's functions. Overall, this approach of using Marchenko wavefields as data in the inversion appears to be prone to artefacts and does, in our experience, not lead to beneficial results. This strategy might, however, work better for density inversion or when incorporated advantageously in a parallel Marchenko and full waveform inversion scheme.

This paper represents a first step towards using Marchenko methods for improving the kernel of full waveform inversion. These first results underline that using Marchenko-based wavefields rather than

Downloaded from https://academic.oup.com/gji/article/234/1/228/7036769 by Centrum voor wiskunde en Informatica user on 05 June 2023

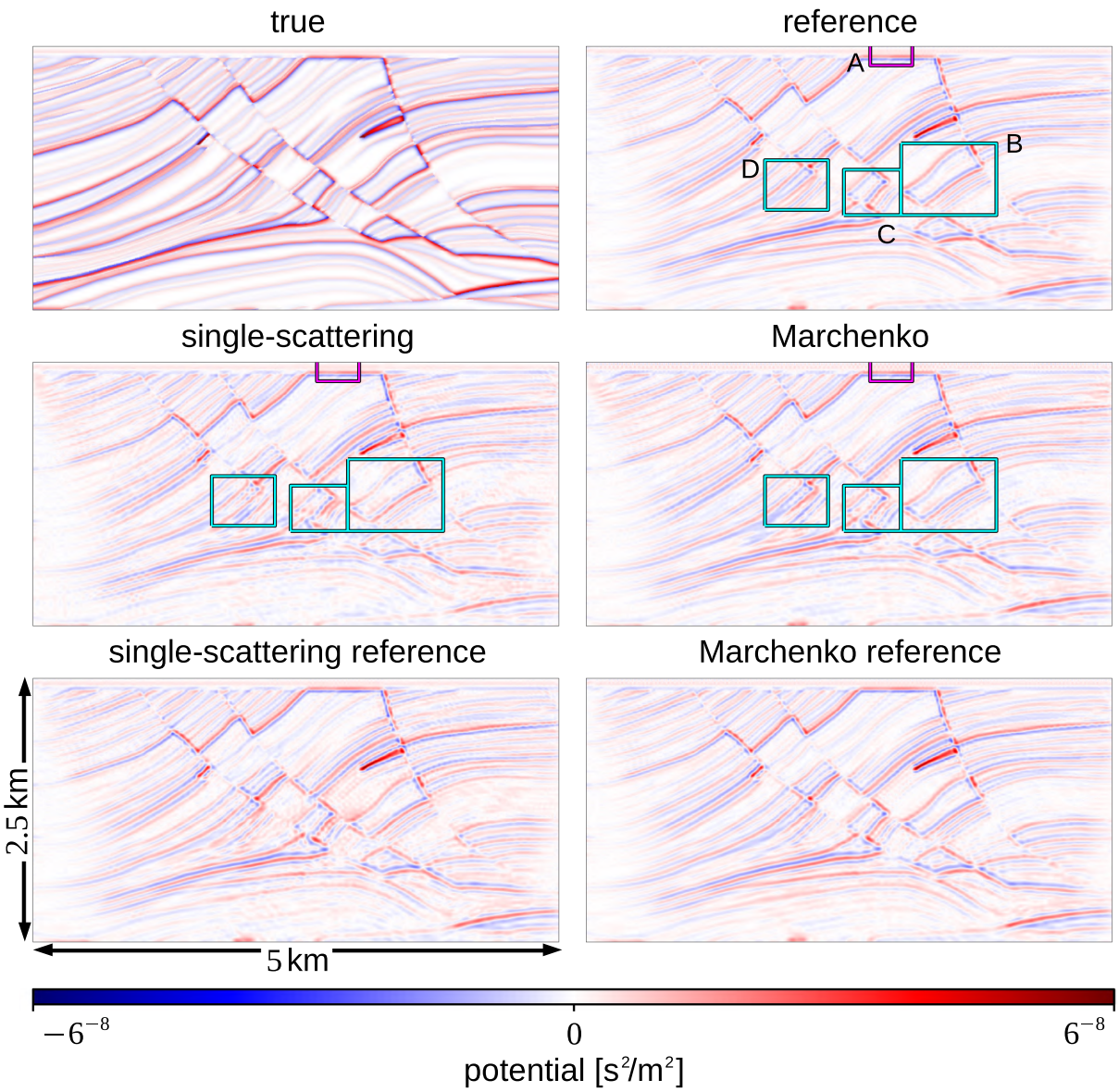

Figure 9. Scattering potentials for the true model in Fig. 2 and background model B, Fig. 5. The true potential (top left) follows from eq. (8). The five inverted potentials are for the different kernels in Table 2. All inversion results are for a regularisation parameter $\beta = 10^{22}$. The magenta box denotes artefacts in the Marchenko solution. Cyan boxes denote areas where the Marchenko result is better than the single-scattering result. See Fig. 10 for zoomed boxes.

a single-scattering assumption can deliver slightly superior inversion results.

7 CONCLUSION

We present a Marchenko-linearised full waveform inversion scheme. While conventional inversion strategies rely on a Born approximation to obtain a model update, our method uses Marchenko-based Green's functions to linearise the inverse problem. We demonstrate how the theory for Marchenko-based Green's function retrieval and gradient computations in full waveform inversion are connected. Marchenko-based Green's functions rely on prior knowledge of the first arrivals of the Green's functions. These first arrivals are usually obtained by modelling in a background medium. Our numerical examples demonstrate that the quality of the first arrivals of the Green's functions is crucial for the success of Marchenko-linearised full waveform inversion. While our scheme delivers slightly better inversion results than the single-scattering approximation when using the same background model, a correct first arrival Green's function allows for near-perfect inversion results. Hence, we illustrate the possibilities and limitations of Marchenko-linearisation and hope that this will help future research in developing efficient and superior imaging methods.

ACKNOWLEDGMENTS

The authors are very grateful to Roel Snieder, Joost van der Neut, Aydin Shoja, Dominic Cummings and Andrew Curtis for fruitful discussions and feedback. Furthermore, the authors acknowledge the constructive feedback from Kees Wapenaar and Polina Zheglova that helped to improve this manuscript. Leon Diekmann was financially supported by the Utrecht Consortium for Subsurface Imaging (UCSI).

Downloaded from https://academic.oup.com/gji/article/234/1/228/7036769 by Centrum voor wiskunde en Informatica user on 05 June 2023

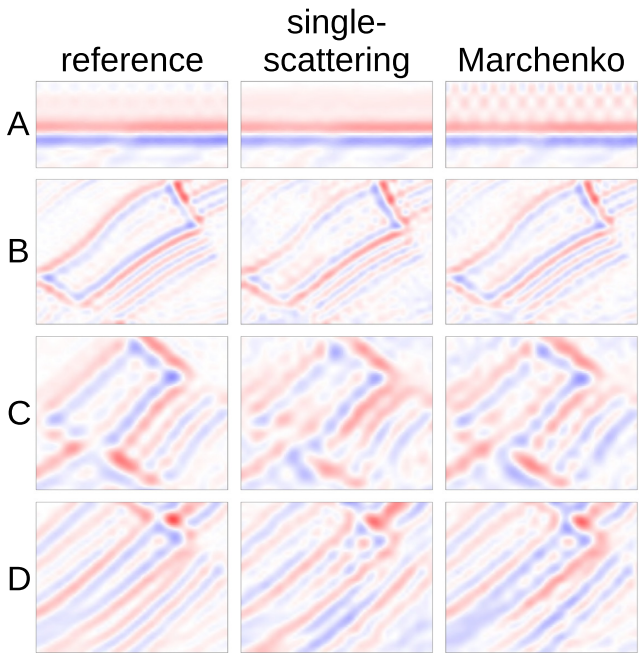

Figure 10. Zoomed versions of the highlighted areas in Fig. 9. The letters A, B, C and D refer to the different boxes, see Fig. 9. We show these zoomed images for the reference kernel, the single-scattering kernel and the Marchenko kernel, see Table 2.

DATA AVAILABILITY

No data were used for this study. The code that was developed for the paper can be shared upon justified request to the corresponding author.

REFERENCES

Bernard, S., Monteiller, V., Komatitsch, D. & Lasaygues, P., 2017. Ultrasonic computed tomography based on full-waveform inversion for bone quantitative imaging, *Phys. Med. Biol.,* **62**(17), 7011.

Born, M. & Wolf, E., 1953. *Principles of Optics,* Pergamon Press, UK.

Broggini, F., Snieder, R. & Wapenaar, K., 2012. Focusing the wavefield inside an unknown 1D medium: Beyond seismic interferometry, *Geophysics,* **77**(5), A25–A28.

Broggini, F., Snieder, R. & Wapenaar, K., 2014. Data-driven wavefield focusing and imaging with multidimensional deconvolution: Numerical examples for reflection data with internal multiples, *Geophysics,* **79**(3), WA107–WA115.

Burridge, R., 1980. The Gelfand-Levitan, the Marchenko and the Gopinath-Sondhi integral equations of inverse scattering theory, regarded in the context of inverse impulse-response problems, *Wave Motion,* **2**(4), 305–323.

Cui, T., Rickett, J., Vasconcelos, I. & Veitch, B., 2020. Target-oriented full-waveform inversion using Marchenko redatumed wavefields, *Geophys. J. Int.,* **223**(2), 792–810.

Dai, W., Fowler, P. & Schuster, G.T., 2012. Multi-source least-squares reverse time migration, *Geophys. Prospect.,* **60,** 681–695 (4-Simultaneous Source Methods for Seismic Data), doi:10.1111/j.1365-2478.2012.01092.x.

De Ridder, S. & Curtis, A., 2017. Seismic gradiometry using ambient seismic noise in an anisotropic Earth, *Geophys. J. Int.,* **209**(2), 1168–1179.

Diekmann, L. & Vasconcelos, I., 2020. Imaging with the exact linearised Lippmann–Schwinger integral by means of redatumed in-volume wavefields, *SEG International Exposition and Annual Meeting,* OnePetro, Houston, USA, doi:10.1190/segam2020-3411883.1.

Diekmann, L. & Vasconcelos, I., 2021. Focusing and Green's function retrieval in three-dimensional inverse scattering revisited: A single-sided Marchenko integral for the full wave field, *Phys. Rev. Res.,* **3**(1), 013206, doi:10.1103/PhysRevResearch.3.013206.

Diekmann, L., Vasconcelos, I., Cummings, D. & Curtis, A., 2021. Towards exact linearized full-waveform inversion via Marchenko redatuming, *SEG/AAPG/SEPM First International Meeting for Applied Geoscience & Energy,* OnePetro, Houston, USA, doi:10.1190/segam2021-3583558.1.

Diekmann, L., Vasconcelos, I., Wapenaar, K., Slob, E. & Snieder, R., 2022. Wavefield focusing using a generalised, potentially asymmetric homogeneous green's function, *Wave Motion,* 103071, doi:10.1016/j.wavemoti.2022.103071.

Engquist, B. & Yang, Y., 2022. Optimal transport based seismic inversion: Beyond cycle skipping, *Commun. Pure appl. Math.,* **75**(10), 2201–2244.

Fokkema, J.T. & van den Berg, P.M., 1993. *Seismic Applications of Acoustic Reciprocity,* Elsevier, the Netherlands, ISBN:0-444 89044 0.

Grohmann, M., Müller, S., Niederleithinger, E. & Sieber, S., 2017. Reverse time migration: Introducing a new imaging technique for ultrasonic measurements in civil engineering, *Near Surface Geophys.,* **15**(3), 242–258.

Guasch, L., Calderón Agudo, O., Tang, M.-X., Nachev, P. & Warner, M., 2020. Full-waveform inversion imaging of the human brain, *NPJ Digit. Med.,* **3**(1), 1–12.

Huang, G., Nammour, R. & Symes, W.W., 2018. Volume source-based extended waveform inversion, *Geophysics,* **83**(5), R369–R387.

Lippmann, B.A. & Schwinger, J., 1950. Variational principles for scattering processes. i, *Phys. Rev.,* **79**(3), 469, doi:10.1103/PhysRev.79.469.

Malcolm, A.E., Ursin, B. & De Hoop, M.V., 2009. Seismic imaging and illumination with internal multiples, *Geophys. J. Int.,* **176**(3), 847–864.

Meles, G.A., Löer, K., Ravasi, M., Curtis, A. & da Costa Filho, C.A., 2015. Internal multiple prediction and removal using Marchenko autofocusing and seismic interferometry, *Geophysics,* **80**(1), A7–A11.

Métivier, L., Brossier, R., Merigot, Q. & Oudet, E., 2019. A graph space optimal transport distance as a generalization of lp distances: application to a seismic imaging inverse problem, *Inverse Probl.,* **35**(8), 085001, doi:10.1088/1361-6420/ab206f.

Paige, C.C. & Saunders, M.A., 1982. Lsqr: An algorithm for sparse linear equations and sparse least squares, *ACM Trans. Math. Softw.,* **8**(1), 43–71.

Ravasi, M., Vasconcelos, I., Kritski, A., Curtis, A., Filho, C.A.D.C. & Meles, G.A., 2016. Target-oriented Marchenko imaging of a North Sea field, *Geophys. Suppl. Mon. Not. R. Astron. Soc.,* **205**(1), 99–104.

Rawlinson, N., Pozgay, S. & Fishwick, S., 2010. Seismic tomography: a window into deep Earth, *Phys. Earth planet. Inter.,* **178**(3–4), 101–135.

Revelo, D., De Paula, R., Pestana, R., Santos, R., Barrera, D. & Souza, M., 2022. A least-squares formulation to solve the single-sided Marchenko integral for the full wave field, *83rd EAGE Annual Conference & Exhibition,* Vol. **2022,** pp. 1–5, European Association of Geoscientists & Engineers, the Netherlands, doi:10.3997/2214-4609.202210825.

Rose, J.H., 2001. "single-sided" focusing of the time-dependent Schrödinger equation, *Phys. Rev. A,* **65**(1), 012707, doi:10.1103/PhysRevA.65.012707.

Schuster, G.T. *et al.*, 2009. *Seismic Interferometry,* Vol. **1,** Cambridge Univ. Press, Cambridge

Shoja, S.A., Meles, G.A. & Wapenaar, K., 2020. A proposal for Marchenko-based target-oriented full waveform inversion, *EAGE 2020 Annual Conference & Exhibition Online,* Vol. **2020,** pp. 1–5, European Association of Geoscientists & Engineers, the Netherlands, doi:10.3997/2214-4609.202011020.

Shoja, S., Van der Neut, J. & Wapenaar, K., 2022. Reducing the overburden-related artifacts in target-oriented least-squares migration by Marchenko double-focusing, *83rd EAGE Annual Conference & Exhibition,* Vol. **2022,** pp. 1–5, European Association of Geoscientists & Engineers, doi:10.3997/2214-4609.202210258.

Snieder, R. & Van Wijk, K., 2015. *A Guided Tour of Mathematical Methods for the Physical Sciences,* Cambridge Univ. Press, Cambridge.

Tarantola, A., 1984. Inversion of seismic reflection data in the acoustic approximation, *Geophysics,* **49**(8), 1259–1266.

van der Neut, J., Thorbecke, J., Wapenaar, K. & Slob, E., 2015a. Inversion of the multidimensional Marchenko equation, *77th EAGE Conference and Exhibition 2015,* Vol. **2015,** pp. 1–5, European Association of Geoscientists & Engineers, doi:10.3997/2214-4609.201412939.

Downloaded from https://academic.oup.com/gji/article/234/1/228/7036769 by Centrum voor wiskunde en Informatica user on 05 June 2023

van der Neut, J., Vasconcelos, I. & Wapenaar, K., 2015b. On Green's function retrieval by iterative substitution of the coupled Marchenko equations, *Geophys. J. Int.,* **203**(2), 792–813.
van Leeuwen, T., 2019. *A Note on Extended Full Waveform Inversion,* preprint (arXiv:1904.00363).
Vargas, D., Vasconcelos, I., Sripanich, Y. & Ravasi, M., 2021. Scattering-based focusing for imaging in highly complex media from band-limited, multicomponent data, *Geophysics,* **86**(5), WC141–WC157.
Vasconcelos, I., Snieder, R. & Douma, H., 2009. Representation theorems and Green's function retrieval for scattering in acoustic media, *Phys. Rev. E,* **80**(3), 036605, doi:10.1103/PhysRevE.80.036605.
Virieux, J. & Operto, S., 2009. An overview of full-waveform inversion in exploration geophysics, *Geophysics,* **74**(6), WCC1–WCC26.
Virieux, J., Asnaashari, A., Brossier, R., Métivier, L., Ribodetti, A. & Zhou, W., 2017. An introduction to full waveform inversion, *Encyclopedia of Exploration Geophysics,* pp. R1–1, Society of Exploration Geophysicists, doi:10.1190/1.9781560803027.entry6.
Wang, G., Guo, Q., Alkhalifah, T. & Wang, S., 2020. Frequency-domain least-squares generalized internal multiple imaging with the energy norm, *Geophysics,* **85**(4), S233–S240.
Wapenaar, K., Broggini, F., Slob, E. & Snieder, R., 2013. Three-dimensional single-sided Marchenko inverse scattering, data-driven focusing, Green's function retrieval and their mutual relations, *Phys. Rev. Letters,* **110**(8), 084301, doi:10.1103/PhysRevLett.110.084301.
Wapenaar, K., Thorbecke, J., Van Der Neut, J., Broggini, F., Slob, E. & Snieder, R., 2014. Marchenko imaging, *Geophysics,* **79**(3), WA39–WA57.
Warner, M. & Guasch, L., 2016. Adaptive waveform inversion: Theory, *Geophysics,* **81**(6), R429–R445.
Warner, M. *et al.*, 2013. Anisotropic 3D full-waveform inversion, *Geophysics,* **78**(2), R59–R80.
Yao, G. & Jakubowicz, H., 2012. Non-linear least-squares reverse-time migration, *2012 SEG Annual Meeting,* OnePetro, doi:10.1190/segam2012-1435.1.
Yao, G., Wu, D. & Wang, S.-X., 2020. A review on reflection-waveform inversion, *Pet. Sci.,* **17**(2), 334–351.
Zhang, D. & Schuster, G.T., 2014. Least-squares reverse time migration of multiples, *Geophysics,* **79**(1), S11–S21.
Zuberi, M. & Alkhalifah, T., 2014. Generalized internal multiple imaging, *Geophysics,* **79**(5), S207–S216.

APPENDIX

In this section we demonstrate how both the Lippmann–Schwinger integral as well as the Marchenko-type integral are related to Rayleigh's reciprocity theorem.

Rayleigh's reciprocity theorem

Rayleigh's reciprocity theorem for acoustic waves reads (Fokkema & van den Berg 1993; Vasconcelos *et al.* 2009)

$$\int_{\tilde{\boldsymbol{x}}\in\partial V} (u^A \boldsymbol{v}^B - u^B \boldsymbol{v}^A)\cdot \mathrm{d}\boldsymbol{S} = \int_{\boldsymbol{x}\in V} \boldsymbol{f}^A\cdot\boldsymbol{v}^B + s^B u^A - \boldsymbol{f}^B\cdot\boldsymbol{v}^A - s^A u^B \,\mathrm{d}V + \int_{\boldsymbol{x}\in V} i\omega(\kappa^B-\kappa^A)u^A u^B - i\omega(\rho^B-\rho^A)\boldsymbol{v}^A\cdot\boldsymbol{v}^B\,\mathrm{d}V\,, \quad \text{(A1)}$$

where A and B mark two different wave states. The pressure field is given by $u = u(\boldsymbol{x},\omega)$, the particle velocity field by $\boldsymbol{v} = (v_1, v_2, v_3) = \boldsymbol{v}(\boldsymbol{x},\omega)$. The variable $\boldsymbol{f} = (f_1, f_2, f_3) = \boldsymbol{f}(\boldsymbol{x},\omega)$ denotes the volume force density source, while $s = s(\boldsymbol{x},\omega)$ is the volume injection rate density source. The compressibility is $\kappa = \kappa(\boldsymbol{x}) = \rho^{-1}(\boldsymbol{x})c^{-2}(\boldsymbol{x})$.

Lippmann–Schwinger integral

In order to derive the Lippmann–Schwinger integral from eq. (A1), we are going to use the following scenario: the density is the same in both wave states, there are no force sources, one state is for the Green's function and the other for the background Green's function, i.e.

$$\rho^A = \rho^B = \rho\,, \quad \text{(A2)}$$

$$\boldsymbol{f}^A = \boldsymbol{f}^B = \boldsymbol{0}\,, \quad \text{(A3)}$$

$$s^A = \delta(\boldsymbol{x}-\boldsymbol{x_s}),\ \ \kappa^A = \rho^{-1}c^{-2}(\boldsymbol{x}),\ \ u^A = g(\boldsymbol{x},\omega;\boldsymbol{x_s}), \quad \text{(A4)}$$

$$s^B = \delta(\boldsymbol{x}-\boldsymbol{x_r}),\ \ \kappa^B = \rho^{-1}c_0^{-2}(\boldsymbol{x}),\ \ u^B = g_0(\boldsymbol{x},\omega;\boldsymbol{x_r}). \quad \text{(A5)}$$

From eq. (A3) it follows that $\boldsymbol{v} = (\rho i\omega)^{-1}\nabla u$. Furthermore, we assume, e.g. Sommerfeld radiation conditions on the boundary ∂V of the volume V such that the left-hand side of eq. (A1) vanishes. Hence, $\boldsymbol{x_s}$ and $\boldsymbol{x_r}$ as well as all perturbations of the model $c(\boldsymbol{x})$ with respect to the model $c_0(\boldsymbol{x})$ lie within the bounded volume V. Eq. (A1) then becomes

$$0 = g(\boldsymbol{x_r},\omega;\boldsymbol{x_s}) - g_0(\boldsymbol{x_s},\omega;\boldsymbol{x_r}) + \int_{\boldsymbol{x}\in V} \frac{i\omega}{\rho}\left(\frac{1}{c_0^2(\boldsymbol{x})} - \frac{1}{c^2(\boldsymbol{x})}\right) g(\boldsymbol{x},\omega;\boldsymbol{x_s})g_0(\boldsymbol{x},\omega;\boldsymbol{x_r})\,dV\,. \quad \text{(A6)}$$

Using source-receiver reciprocity, that is $g_0(\boldsymbol{x_s},\omega;\boldsymbol{x_r}) = g_0(\boldsymbol{x_r},\omega;\boldsymbol{x_s})$, this delivers the Lippmann–Schwinger integral, eq. (6).

Integral form of the homogeneous Green's function of the second kind

In order to derive a Marchenko-type integral from eq. (A1), we are going to use the following scenario: both density and velocity are identical in the two wave states, there are no force sources, one state is for the Green's function and one for the homogeneous Green's function of the second kind, i.e.

$$\rho^A = \rho^B = \rho\,, \quad \text{(A7)}$$

$$\kappa^A = \kappa^B = \rho^{-1}c^{-2}(\boldsymbol{x})\,, \quad \text{(A8)}$$

$$\boldsymbol{f}^A = \boldsymbol{f}^B = \boldsymbol{0}\,, \quad \text{(A9)}$$

$$s^A = \delta(\boldsymbol{x}-\boldsymbol{x_s})\,, \quad u^A = g(\boldsymbol{x},\omega;\boldsymbol{x_s}) \quad \text{(A10)}$$

$$s^B = 0\,, \quad u^B = g(\boldsymbol{x},\omega;\boldsymbol{x_f}) + f(\boldsymbol{x},\omega;\boldsymbol{x_f}) - f^*(\boldsymbol{x},\omega;\boldsymbol{x_f})\,. \quad \text{(A11)}$$

As we consider the same medium in both wave states (same compressibility and density), the second volume integral in eq. (A1) vanishes. From eq. (A9) we get $\boldsymbol{v} = (\rho i\omega)^{-1}\nabla u$. This gives

$$\frac{1}{\rho i\omega}\int_{\tilde{\boldsymbol{x}}\in\partial V} \left(g(\tilde{\boldsymbol{x}},\omega;\boldsymbol{x_s})\nabla u^B - u^B\nabla g(\tilde{\boldsymbol{x}},\omega;\boldsymbol{x_s})\right)\cdot \mathrm{d}\boldsymbol{S} = -\left(g(\boldsymbol{x_s},\omega;\boldsymbol{x_f}) + f(\boldsymbol{x_s},\omega;\boldsymbol{x_f}) - f^*(\boldsymbol{x_s},\omega;\boldsymbol{x_f})\right). \quad \text{(A12)}$$

While $g(\tilde{\boldsymbol{x}},\omega;\boldsymbol{x_s})$ is a purely causal (out-going) wavefield with respect to the volume V for $\boldsymbol{x_s}$ in V, u^B contains both causal, i.e. $u^B_{out} = g(\tilde{\boldsymbol{x}},\omega;\boldsymbol{x_f}) + f(\tilde{\boldsymbol{x}},\omega;\boldsymbol{x_f})$ and anticausal (in-coming), i.e. $u^B_{in} = -f^*(\tilde{\boldsymbol{x}},\omega;\boldsymbol{x_f})$, contributions for $\boldsymbol{x_f}$ in V. Using, e.g. a far-field approximation (Schuster *et al.* 2009), we find that $g(\tilde{\boldsymbol{x}},\omega;\boldsymbol{x_s})\nabla u^B_{out} = u^B_{out}\nabla g(\tilde{\boldsymbol{x}},\omega;\boldsymbol{x_s})$ and $g(\tilde{\boldsymbol{x}},\omega;\boldsymbol{x_s})\nabla u^B_{in} = -u^B_{in}\nabla g(\tilde{\boldsymbol{x}},\omega;\boldsymbol{x_s})$ leading

Downloaded from https://academic.oup.com/gji/article/234/1/228/7036769 by Centrum voor wiskunde en Informatica user on 05 June 2023

to

$$\frac{2}{\rho i\omega}\int_{\tilde{\boldsymbol{x}}\in\partial V} f^*(\tilde{\boldsymbol{x}},\omega;\boldsymbol{x_f})\nabla g(\tilde{\boldsymbol{x}},\omega;\boldsymbol{x_s})\cdot \mathrm{d}\boldsymbol{S} = -\big(g(\boldsymbol{x_s},\omega;\boldsymbol{x_f}) + f(\boldsymbol{x_s},\omega;\boldsymbol{x_f}) - f^*(\boldsymbol{x_s},\omega;\boldsymbol{x_f})\big)\,. \tag{A13}$$

If $\boldsymbol{x_s}$ is close to the boundary ∂V, above equation will only reconstruct the out-going portion of the wavefield u^β on the right-hand side,

$$-\frac{2}{\rho i\omega}\int_{\tilde{\boldsymbol{x}}\in\partial V} f^*(\tilde{\boldsymbol{x}},\omega;\boldsymbol{x_f})\nabla g(\tilde{\boldsymbol{x}},\omega;\boldsymbol{x_s})\cdot \mathrm{d}\boldsymbol{S} = g(\boldsymbol{x_s},\omega;\boldsymbol{x_f}) + f(\boldsymbol{x_s},\omega;\boldsymbol{x_f})\,. \tag{A14}$$

Finally, we split the boundary ∂V into two parts: a horizontal boundary ∂V_0 at $x_3 = 0$ and a half-sphere ∂V_1 below, i.e. for $x_3 > 0$ and a downwards-pointing x_3-axis. Assuming that the focusing function $-f^*(\boldsymbol{x},\omega;\boldsymbol{x_f})$ vanishes for all $\boldsymbol{x} \in \partial V_1$, we only keep the integral over ∂V_0. Note that this requires very particular sources $q(\boldsymbol{x},\omega)$ in eq. (12), but we will not explicitly write this dependency here in the arguments of the focusing function. Using these additional assumptions in eq. (A14) gives eq. (15).

Downloaded from https://academic.oup.com/gji/article/234/1/228/7036769 by Centrum voor wiskunde en Informatica user on 05 June 2023